



HAL
open science

Morphological and magnetic study of plasma assisted solid-state dewetting of ultra-thin cobalt films on conductive titanium silicon nitride supports

A. Andalouci, O. Brinza, C. Porosnicu, C. Lungu, Frédéric Mazaleyrat, Y. Roussigné, S.M. Chérif, S. Farhat

► To cite this version:

A. Andalouci, O. Brinza, C. Porosnicu, C. Lungu, Frédéric Mazaleyrat, et al.. Morphological and magnetic study of plasma assisted solid-state dewetting of ultra-thin cobalt films on conductive titanium silicon nitride supports. *Thin Solid Films*, 2020, 703, pp.137973. 10.1016/j.tsf.2020.137973 . hal-03490266

HAL Id: hal-03490266

<https://hal.science/hal-03490266>

Submitted on 20 May 2022

HAL is a multi-disciplinary open access archive for the deposit and dissemination of scientific research documents, whether they are published or not. The documents may come from teaching and research institutions in France or abroad, or from public or private research centers.

L'archive ouverte pluridisciplinaire **HAL**, est destinée au dépôt et à la diffusion de documents scientifiques de niveau recherche, publiés ou non, émanant des établissements d'enseignement et de recherche français ou étrangers, des laboratoires publics ou privés.



Distributed under a Creative Commons Attribution - NonCommercial 4.0 International License

Morphological and magnetic study of plasma assisted solid-state dewetting of ultra-thin cobalt films on conductive titanium silicon nitride supports

A. Andalouci¹, O. Brinza¹, C. Porosnicu², C. Lungu², F. Mazaleyrat³, Y. Roussigné¹, S. M. Chérif¹, and S. Farhat^{1,a)}

¹Laboratoire des Sciences des Procédés et des Matériaux, CNRS, LSPM – UPR 3407, Université Paris 13, PRES Sorbonne-Paris-Cité, Villetaneuse, 93430, France

² National Institute for Laser, Plasma and Radiation Physics, NILPRP, RO-077125, Bucharest, Romania

³ Laboratoire SATIE, ENS Paris-Saclay, Cachan, 94230, France

Abstract

Since metals are high-surface energy materials, it is difficult to stabilize metal nanoparticles on conductive substrates, on the other side, producing nanoparticles on low surface energy oxides is hindered by high temperature activated phenomena such as diffusion on the surface as well as in the bulk. In this work, we present a simple and efficient approach to produce controlled cobalt (Co) magnetic nanoparticles by solid state dewetting of sub 3 nm metal films deposited on conductive and low surface energy titanium silicon nitride (TiSiN) barriers. For this purpose, ultrathin Co films with thickness of 1, 2 and 3 nm were first deposited on the top of the TiSiN layer; then Co films were submitted to different variations of dewetting protocols. Solid state dewetting process will be analyzed from kinetic and thermodynamic points of view. Structural and magnetic characterizations of the patterned nanoparticles showed that the size, the density and the structure of the generated nanoparticles are well controlled using TiSiN barrier and plasma treatment. The magnetic measurements showed relatively high coercivity and confirmed that dewetting parameters can be used to tune the design of nanoparticles and their size distribution on TiSiN substrates, thereby providing a promising tool to control their coercive field.

Keywords: Solid state dewetting; plasma-induced dewetting; Cobalt nanoparticles; Titanium silicon nitride; Magnetic properties.

^{a)}Corresponding author: farhat@lspm.cnrs.fr

1. Introduction

Metallic nanoparticles (MNPs) are considered to be the building blocks for many nanotechnology based devices [1]. The study of such materials structure and properties is therefore of great fundamental interest, especially since physio-chemical properties of MNPs are governed by their structure. Indeed, both equilibrium and non-equilibrium magnetic properties of cobalt NPs, depend on geometrical parameters such as particle size and shape. Consequently, the coercive field value H_c of the NPs is size and shape dependent [1-5]. MNPs can be disposed on a substrate and integrated in electronic and photonic devices fabrications[6, 7], bio-sensing [8], catalysis [9], and data storage applications [10, 11]. Moreover the surface density of these MNPs on a substrate is an important factor which must be considered for catalyzing carbon nanotubes growth [12], and to control their behavior as an assembly for the fabrication of metamaterials [13]. However the control of these parameters on the nanoscale level is hampered by high cost techniques such as lithography [14], thereby, other innovative techniques have been developed to engineer these nanostructures such as nanoembedding [9], spatially confined dewetting [15] or templated dewetting [16]. In this sense, solid state dewetting of thin metal films is a promising strategy for MNPs controlled fabrication oriented towards different applications as represented in figure 1.

Solid-state dewetting is a common undesirable phenomenon found in thin film devices caused by heating leading their degradation and failure [17]. However, it could be also intentionally used as an effective cost friendly process to form ordered arrays of self-organized nanoparticles on a desired substrate [18, 19]. This process is driven by the difference in surface energy of the thin film and the underlying support and could be industrially scalable to morphologically transform continuous films (Cu [20], Au [21], Ag [22], Pt [23], Sn [24], Co [25]) into islands or droplets used to produce Nano devices. The nature of the substrate is a crucial factor in controlling these arrays and can vary depending on the desired application from semiconductors (Si [26, 27], Ge[28]), insulators (SiO₂ [20, 29, 30], Al₂O₃ [31-33], ZrO₂ [34], MgO [35], Si₃N₄ [36]) or conductive alloys (TiSiN [37], TiN [38], AlSi [39], CoSi₂ [40]).

Solid state dewetting has the same origin as the dewetting of liquids *i.e.* a reduction of the energy of the surface/interface by shape change of the film. Indeed, continuous metallic films are metastable when deposited on a substrate they do not wet. Their spontaneous evolution when thermally annealed at sufficiently high temperatures, results in very specific nanostructures. Annealing temperature is sometimes well below the film's melting temperature but could occur also above the melting temperature of the material, if laser irradiation [41, 42] or ion irradiation [43] are used. The physics of this morphological instability is quite different in the case of

solids where the transport of atoms is caused by surface diffusion rather than by hydrodynamic flow as in liquids, the knowledge of diffusion paths is crucial since diffusive mass transport can occur along the surface, the interface or grain boundaries to form what was called by “grooves”, finally the propagation of these grooves results the formation of dispersed nanoparticles ideally of a spherical shape. This equilibrium shape of the nanoparticle (indexed “1”) with a surface energy γ_1 on a substrate (indexed “2” as substrate) with a surface energy γ_2 is described by the Young-Laplace equation [19]:

$$\gamma_2 = \gamma_{12} + \gamma_1 \cos\theta \quad (1)$$

Where γ_{12} is the energy of the nanoparticle-substrate interface and θ is the equilibrium contact angle. The balance of these three interfacial tensions is illustrated in Figure 1. If $\gamma_2 > \gamma_{12} + \gamma_1$, the film will be stable and will not dewett. However if this condition is not satisfied, the film will dewett due to thermal annealing. In this case, atoms are sufficiently activated to overcome the energy barrier. The wettability of a given metal can be evaluated by the contact angle θ . Good wettability is insured when contact angle is smaller than 90° and the wettability becomes weak for a contact angle larger than 90° . The contact angle depends on the nanoparticle and substrate surface energies and could be affected by chemical reactions between liquid alloy and solid substrate as well as surface roughness [44]. Dewetting could be controlled by several parameters including : the initial film thickness [45], the annealing temperature [46] and treatment time [47] leading to controlled nanoparticle size and spacing.

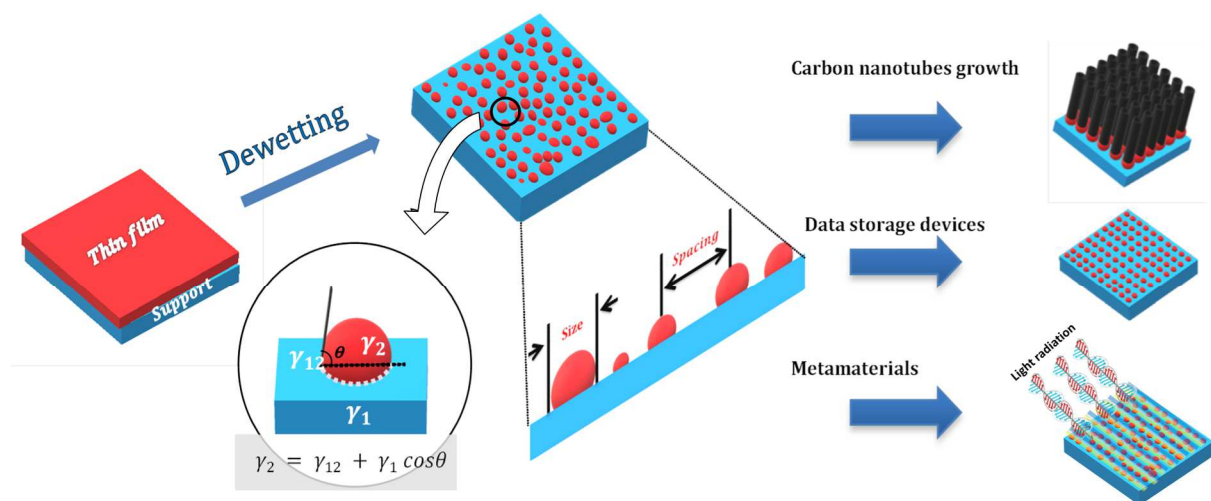


FIG. 1. Scheme of the dewetting process of continuous metal films into isolated nanoparticles and possible applications in nano-electronics.

Depending of its thickness, a flat film may dewett by hole nucleation on defects which is a random process that occur for relatively thick films, or by spinodal surface instability [48] resulting in specific dewetting patterns. Solid-state dewetting is indeed governed by the initial film thickness, Nuryadi *et al.* have demonstrated that the height h and the diameter d of agglomerated Si islands, as well as their surface density, are a function of the initial Si thickness [49]. Moreover experimental results indicate that, whatever the experimental conditions are, dewetting is closely related to the initial thickness of the films, with linear variation in the case of hole nucleation and growth [50, 51], and a $5/3$ power variation in the case of spinodal dewetting [24, 52], the density of nanoparticles varies as a function of the inverse of the square of the initial thickness of the films, h^{-2} . Three models are found in literature to calculate the size and density of dewetted nanoparticles:

Mullins's model

The general theoretical framework describing solid state dewetting was put by Mullins in the 1950s and was called "thermal grooving" [53], Mullins proposed two distinct theories. The first is based on evaporation-condensation and the other on surface diffusion. The depth d of grain boundary groove for evaporation-condensation kinetics and surface diffusion mechanism was calculated by solving total mass conservation. For the case of evaporation-condensation, the groove depth d (i.e., the distance from the groove root to the plane of the initial flat surface) vary with the square root of the time,

$$d = 1.13 \tan(\theta) \sqrt{\alpha t} \quad (2)$$

While for the case of diffusion, atoms diffuse on the surface away from the triple junction, and d scales with the fourth root of the time,

$$d = 1.13 \tan(\theta) \sqrt[4]{\beta t} \quad (3)$$

In equations (2) and (3), t is the time, d is the instantaneous depth of grain boundary, h is the film thickness, θ is the angle at the triple point and α and β are constants depending on the temperature and given by :

$$\alpha = \frac{p_0 \gamma_s \Omega^2}{\sqrt{2} \pi M_W k T} \quad (4)$$

$$\beta = \frac{D_s \gamma_s \Omega^2 v}{k T} \quad (5)$$

where p_0 is the metal vapor pressure in equilibrium over the grain boundary, γ_s is the surface-free energy per unit area, Ω is the molecular volume, M_W is the molecular weight, D_s is the coefficient of surface diffusion and v is the number of atoms per unit area.

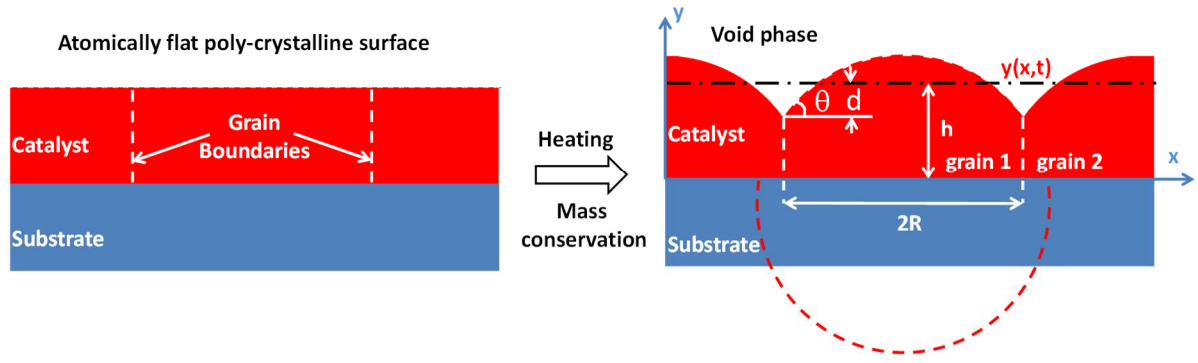


FIG. 2: Schematic cross section of equilibrium circular grain boundary groove formed by heating atomically flat poly-crystalline surface. Time and horizontal coordinate evolution of the free surface area is labelled $y(x,t)$.

Mullins's solution has been proposed to measure interfacial energies and surface diffusivities. Nevertheless, as shown in equations (2) and (3), Mullins's model predicts an unlimited variation of d when the time goes to the infinity.

Srolovitz and Safran model

To overcome this discrepancy in infinite size evolution, Srolovitz and Safran [54], proposed a new model to estimate the equilibrium groove depth for interconnecting spherical shape grain boundaries interacting with each other via surface diffusion. Grains are formed in between internal interfaces called grain boundaries. Due to their high energy in thin solid films, these grain boundaries junctions are primary sites for hole nucleation. Thermodynamic equilibrium requires that the groove angle θ is fixed. Figure 2 shows the equilibrium grain boundary groove configuration in the case of grains in the shape of a circular base with grain radius R and a spherical cap which intersects the grain boundary at an angle θ . The film thickness is h and the equilibrium groove depth, measured with respect to the flat film rushes an equilibrium value given by,

$$d = R \frac{2 - \cos(\theta) + \cos^3(\theta)}{\sin^3(\theta)} \quad (6)$$

For fully dewetting of the film, the groove must intercept the substrate and the groove depth d becomes larger than the film thickness h . However, this model does not consider the effect of initial height h , leading to a nanoparticle size independent of the initial catalyst volume.

Zhong model

In order to consider initial thickness effect, Zhong *et al.* [55] proposed a model based on the conservation of volume as well as the energy of the system before and after nanoparticle formation. Their model considers a truncated sphere formed by dewetting with a surface S_1 in contact with the atmosphere and a surface S_2 in contact with the support. Before the dewetting, the interfacial energy is given by

$$G_1 = A(\gamma_1 + \gamma_{12}) \quad (7)$$

Where γ_1 is the catalyst surface energy, γ_{12} is the catalyst-support surface energy respectively and A is the support area per nanoparticle. After dewetting, the interfacial energy of aspherical nanoparticle of top surface area S_1 and a contact area S_2 is given by:

$$G_2 = (A - S_2)\gamma_2 + S_2\gamma_{12} + S_1\gamma_1 \quad (8)$$

Where S_{12} is the contact area and γ_{12} is the interface surface energy.

By introducing the contact angle θ given by the Young's equation (1) discussed above, and the radius R of the sphere formed by dewetting, we can calculate by geometrical considerations the surfaces S_1 and S_2 :

$$S_1 = 2\pi R^2(1 - \cos\theta) \quad (9)$$

$$S_2 = \pi R^2 \sin^2\theta \quad (10)$$

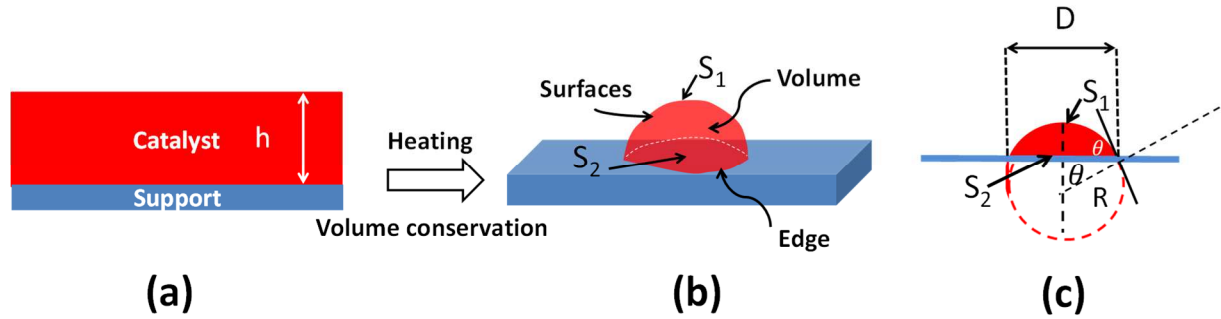


FIG. 3 : (a) Initial catalyst film. (b) Surfaces, volume and edge generated after heating. (c) Schematic cross section considered in Zhong *et al.* model. h : initial film of thickness. S_1 : Top surface area. S_2 : surface of the catalyst in contact with the support. θ : contact angle. R : radius of the hypothetical sphere. D : nanoparticle diameter.

Zhong *et al.* postulate that the minimum particle size occurs at $G_1 = G_2$ and estimated from metal volume conservation the diameter of the nanoparticle D as a function of the initial catalyst thickness h

$$D = \frac{6h \sin \theta}{1 - \cos \theta} \quad \text{for } \theta < 90^\circ \quad (11)$$

$$D = \frac{6h}{1 - \cos \theta} \quad \text{for } \theta > 90^\circ \quad (12)$$

In the other hand, nanoparticle density N could be estimated from contact angle and nanoparticle diameter by the following equations, [81]

$$N = \frac{4(1 + \cos \theta)}{\pi D^2(2 + \cos \theta)} \quad \text{for } \theta < 90^\circ \quad (13)$$

$$N = \frac{4}{\pi D^2(1 - \cos \theta)(2 + \cos \theta)} \quad \text{for } \theta > 90^\circ \quad (14)$$

Nevertheless, the accuracy of this model depends highly on the mitigation of thermally activated processes mainly the migration of catalyst atoms into the bulk of the support and Ostwald ripening at high temperatures

which reduce significantly the efficiency of dewetting process [56]. Indeed, while bulk diffusion is described to lower the size of nanoparticles which is desirable on one part, this loss of mass and its interaction with the underlying substrate causes deactivation of the nanoparticles [56] and the forming of unwanted alloys [57]. On the other hand, larger particles grow in size at the expense of smaller particles and decreases the number density with time, a phenomenon known as Ostwald ripening, which consists of coarsening in which the particle size increases and particle density reduces after extended annealing [58, 59].

In the direction of suppressing these undesirable phenomena, different energy sources can be employed in order to furnish the energy necessary to activate the dewetting process of the film, other than thermal annealing. Many studies have been performed using electron and ion beam irradiation [51, 60, 61], laser induced dewetting [62, 63]. However, little research has been dedicated to plasma-induced dewetting [64]. During plasma treatment, energy is mainly transferred uniformly to the overall surface of the film by accelerated ions that carry more or less equivalent energy [65], which allows the control of nanoparticle size and distribution that depends on the density of radicals and ions which is tuned by plasma power and pressure [66].

While optimizing process conditions helps to control nanoparticles formation, diffusion in the substrate is still considered to be the major problem in dewetting of thin films, many techniques were used to limit diffusion of the dewetted film into the substrate such as the use of metal oxides like SiO_2 and Al_2O_3 as nanoparticles supports; since dewetting is known to proceed easier in substrates of low surface energy than in those of high surface energy. On oxides, diffusion can mostly be mitigated by using multiple step deposition of film to compensate the loss of mass after each heat treatment [67] or by depositing thick films, however, thick films may yield low density and large nanoparticles. Conductive diffusion barriers are more effective solution to work with few nanometers film thickness and especially have been attractive to achieve high area density of nanotubes; Yang *et al.* have proposed to use titanium silicon nitride (TiSiN) supports as a refractory, amorphous, conducting material during nanotube growth from iron catalyst. They showed that TiSiN limits the diffusion of sub-nanometer metallic catalyst (Fe) in the bulk of the underlayer support [37]. Little attention has been paid to this remarkable performance in dewetting ultrathin films. For refractory conductive substrates such TiSiN, there is an application-driven need for producing small dense nanoparticles arrays. TiSiN substrates could also allow a more controllable dewetting, reducing the effect of undesirable processes mentioned earlier. However, little effort has been devoted so far to study the model of dewetting on TiSiN in particular, and conductive substrates in general.

In this work, and based on recent findings, we investigate a range of parameters affecting separately and combined, the dewetting of ultrathin cobalt films and formed nanoparticles properties. The effect of the diffusion barrier, plasma treatment as well the relationship between initial film thickness and dewetted nanoparticles diameter and density will be addressed from structural and magnetic point of views.

2. Material and methods

Substrates of silicon wafers with a (100) polished face were used initially to deposit transition metal nitride layers TiSiN by thermionic vacuum arc (TVA) technology developed at the national institute for laser, plasma and radiation physics in Bucharest, Romania. This technique was proposed by Lungu *et al.* for highly uniform and nanostructured surface coatings deposition and described in detail in [68, 69]. Even several techniques were proposed in the past to produce TiSiN including, physical vapor deposition, magnetic sputtering, ion beam assisted deposition, and chemical vapor deposition [70], TVA technology remain well adapted to alloy film deposition of high purity and good adhesion mainly due to the gas free evaporation in vacuum and the high density of the power per unit surface of the deposited metal. In summary, an electron beam is generated by a heated cathode composed by a tungsten filament. The experiments were conducted by focusing an electron beam by Wehnelt cylinder in the thermoionic setup. Electrons are then accelerated to the anode containing a mixture of powder to be evaporated. In the case of TiSiN barriers, 3 moles of Ti and 1 mole of Si₃N₄ were used as anode. An electrical arc is then ignited between the cathode and the anode containing the powder in order to create a strong local heating. As a consequence, Ti and Si₃N₄ evaporation builds up to the creation of a plasma in order to ensure the formation of high density layer of titanium silicon nitride with a stoichiometry of ~ TiSiN and a thickness of 50 nm, the deposition rate was estimated 1.42 Å/s using a quartz microbalance. For physical vapor deposition of cobalt on TiSiN substrates, we used the electron beam Plassys MEB 550S type evaporator. This set-up is designed to deposit thin metallic layers of thickness between 1 and 20 nm by the evaporation of a cobalt target with a beam of electrons of power 10 kW under vacuum that ensures better purity of the deposited layers and better control of the thickness of each film. For the cobalt, a pressure of the order of 10⁻⁴ Pa was used, to reach a temperature of about 1050 °C. Film thickness of 1, 2 or 3 nm was deposited at a rate of 0.05 nm/s and was monitored with quartz balance equipment.

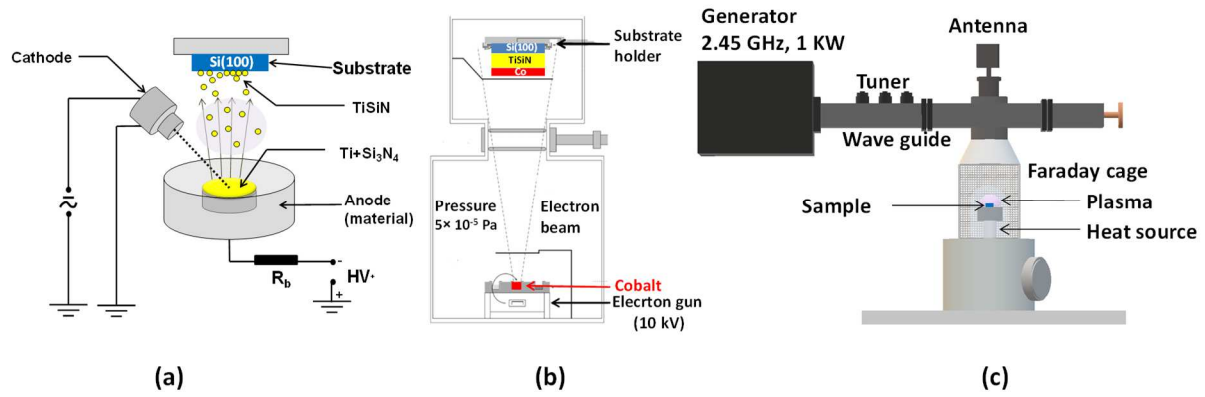


FIG. 4. (a) Thermionic vacuum arc TVA set-up for TiSiN deposition. (b) Electron-beam for cobalt deposition. (c) Microwave plasma enhanced chemical vapor deposition bell jar reactor used for dewetting process.

For dewetting we developed five experimental protocols by using several variants of thermal and/or plasma annealing. In all protocols, hydrogen was used to reduce the residual oxides and to structure the cobalt nanoparticles. Due to the complex nature of a real arrangement of grains composing a film, it is difficult to estimate a priori the time of treatment. Nevertheless, according to Luber et al. [71], no significant changes in film morphology was observed after ~30 min dewetting of nickel films as measured by in situ time resolved reflectometry. Hence, we fixed the final time of treatment from 20 min to 30 min. At the end of each experiment, the plasma, the heater and the gas feeding were switched off to cool down the sample. We performed the 5 protocols discussed above for three catalyst thickness (1, 2 or 3 nm) with (silicon (100) covered by ~2 nm of native oxide (SiO₂) or Titanium silicon nitride TiSiN with a thickness of ~50 nm) acting as nanoparticles support. The samples were labelled S_{ij} or T_{ij} where S and T refers to SiO₂ and TiSiN barriers respectively and i and j refers to the cobalt thickness (1, 2 or 3 nm) and protocol number (1, 2, 3, 4 or 5) respectively. All the other parameters are maintained at their standard values as represented in Figure 5.

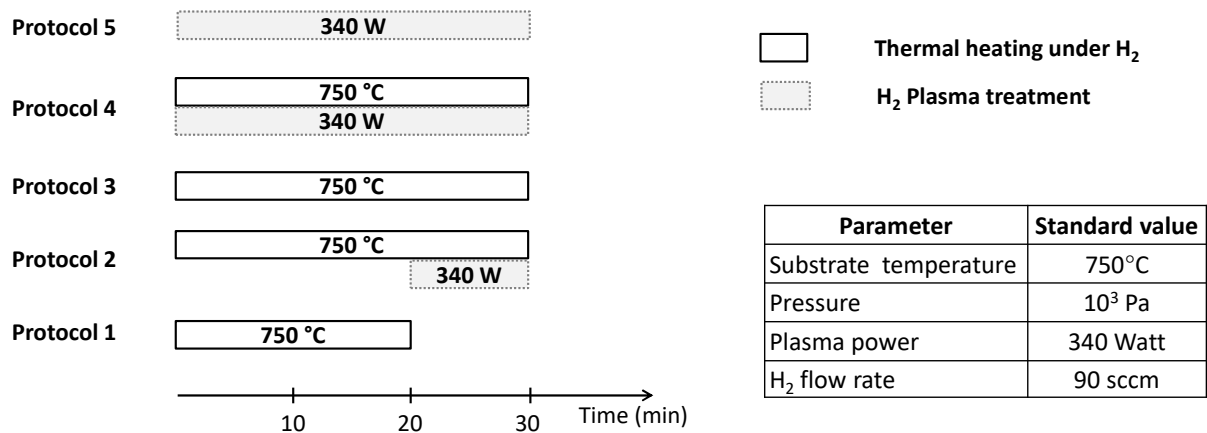


FIG. 5. Experimental protocols and process conditions for cobalt dewetting.

During all the experiments, the substrate temperature was monitored by a dual-wavelength optical pyrometer (IMPAC, IGAQ-10) at $750\pm 5^\circ\text{C}$, and we considered this temperature to be the actual substrate temperature for cobalt dewetting. The surface morphology of cobalt nanoparticles was investigated using scanning electron microscopy (SEM) LEO 440 at an operating voltage of 3 kV. Static magnetic properties were performed using a vibrating sample magnetometer (VSM) Lakeshore 7400 that records the magnetization M versus the applied magnetic field H from -50 mT to 50 mT at a temperature of 300 K.

3. Results and discussion

To investigate the effect of initial layer thickness and the nature of the substrate on the Co dewetting process, Co films deposited on SiO_2 and TiSiN supports were subjected to the protocols discussed above.

3.1 Substrate nature effect

Figure 6a and Figure 6b shows SEM pictures after the dewetting of 3 nm cobalt on TiSiN (sample T₃₁) and SiO_2 (sample S₃₁) barriers using protocol 1. Figure 6c and figure 6d shows SEM pictures of the dewetting of 3 nm cobalt on TiSiN (sample T₃₂) and SiO_2 (sample S₃₂) barriers respectively using protocol 2. These pictures clearly show a spontaneous breakup of the film into visible isolated nanoparticles.

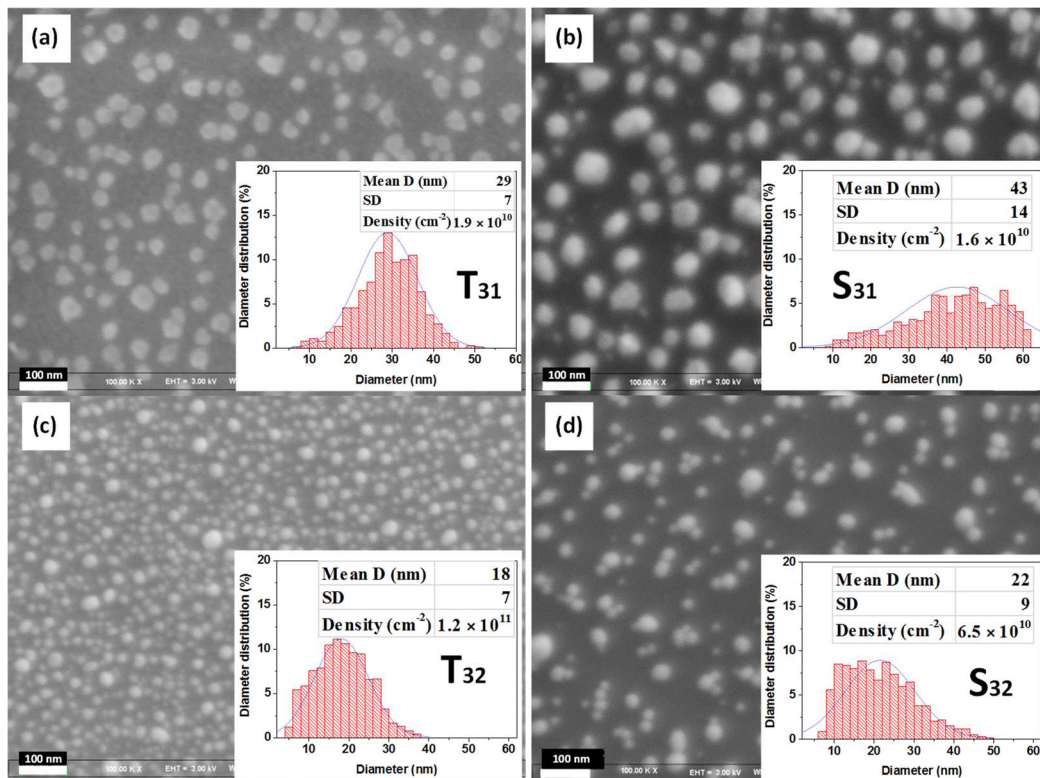


FIG. 6. Top-view SEM images of cobalt nanoparticles formed by dewetting of 3 nm thickness Co films after : protocol 1: (a) Co 3 nm on TiSiN (sample T₃₁), (b) Co 3 nm on SiO_2 (sample S₃₁), protocol 2: (c) Co 3 nm on TiSiN (sample T₃₂), (d) Co 3 nm on SiO_2 (sample S₃₂).

Statistical analysis of these images was performed using ImageJ software and based on at least 300 nanoparticles taken in different regions. This allows the determination of the surface density $N(\text{cm}^{-2})$, and the diameter distribution (nm), as well as the standard deviation SD (nm) as represented in the insert of figure 6. The analysis of these data shows that as compared to SiO_2 , TiSiN barriers improves the surface density by a factor of 25% for thermal annealing of 3 nm Co films, from $1.6 \times 10^{10} \text{ cm}^{-2}$ for SiO_2 to $2 \times 10^{10} \text{ cm}^{-2}$ for TiSiN, and by a factor of ~85% using combined thermal annealing and plasma treatment from $6.5 \times 10^{10} \text{ cm}^{-2}$ for SiO_2 to $1.2 \times 10^{11} \text{ cm}^{-2}$ for TiSiN. In the same time, mean diameter is reduced by a factor of ~48% by thermal annealing, from 43 nm SiO_2 to 29 nm for TiSiN, and by a factor of ~18% by combined thermal and plasma treatment, from 22 nm for SiO_2 to 18 nm for TiSiN. Smaller standard deviations are also obtained with TiSiN barriers leading to narrower size distributions shifted to small nanoparticle sizes. Hence, the benefit of the TiSiN barrier in improving cobalt dewetting is clearly confirmed by higher surface density of the nanoparticles, lower particle diameter and higher homogeneity of the distribution. We can notice that the effect of the barrier is confirmed both for thermal treatment and thermal followed by plasma treatment. By comparing surface energies of TiSiN, SiO_2 and cobalt $\gamma_{\text{TiSiN}} = 0.02 \text{ J} \cdot \text{m}^{-2}$ [72], $\gamma_{\text{SiO}_2} = 0.43 \text{ J} \cdot \text{m}^{-2}$ [73] and $\gamma_{\text{Co}} = 2.22 \text{ J} \cdot \text{m}^{-2}$ [40] respectively, we can see that surface energy difference ($\gamma_{\text{Co}} - \gamma_{\text{TiSiN}} = 2.20 \text{ J} \cdot \text{m}^{-2} > \gamma_{\text{Co}} - \gamma_{\text{SiO}_2} = 1.79 \text{ J} \cdot \text{m}^{-2}$), meaning that the driving force for dewetting is higher for Co on TiSiN than for Co on SiO_2 regardless of the energy source. Another spectacular barrier effect is the reducing of the standard deviation when TiSiN is used as compared to SiO_2 . This could be explained by Ostwald ripening effects on SiO_2 . Indeed, this phenomenon increases the density of the large particles at the expense of the smaller ones thereby increasing the standard deviation of the diameter distribution, which widens the size gap between small particles and larger ones as shown in Figure 6. As proposed by Robertson group, TiSiN has proven to restricts iron atoms mobility which slows down Ostwald repining effects resulting in a small and narrow catalyst particle size distribution[39]. Finally, relatively spherical nanoparticles and more homogeneous size distributions are clearly observed when submitting the samples to the second protocol in comparison to the first protocol, which highlight the role of the plasma treatment regardless of the substrate nature.

3.2 Plasma effect

In order to further investigate the plasma effect, three additional protocols with the same treatment time (P3, P4 and P5 as represented in figure 5) were applied to dewett Co on TiSiN. Figure 7 shows SEM images and

diameter distributions of these samples. From Figure 7a, in protocol 3 it is clear that when the time of thermal annealing was increased to 30 minutes (sample T₃₃), surface density drastically decreases and the average size of nanoparticles is increased, another sign of Ostwald ripening phenomenon that is known to escalate with time. To avoid this effect, simultaneous plasma and thermal treatments in protocol 4 were applied leading to homogeneous nanoparticle sizes as shown in Figure 7b (T₃₄). Nevertheless, our results demonstrate that both surface density and particle size distribution are most enhanced when protocol 2 is applied *i.e.* the plasma is applied after the formation of separate nanoparticles by thermal annealing (sample T₃₂ in Figure 6c), indeed, Bogarets *et al.* proposed recently an understanding on the effect of H radicals present in H₂ plasma on metallic nanoclusters while performing thermal annealing; these H radicals bind strongly with metallic atoms rendering them more stable. As a result, the interaction between these nanoparticles becomes very weak and they cannot coalesce [74]. Finally using only plasma treatment to dewett 3 nm cobalt films (protocol 5) has proven to be insufficient to obtain separate islands in 30 minutes (T₃₅), therefore statistical analysis was not possible, this could be explained by the weak energy furnished to the cobalt film by atomic hydrogen. Indeed, temperature monitoring on the samples surface displayed a very slow slope of rising temperature that reached 350°C at the end of the treatment.

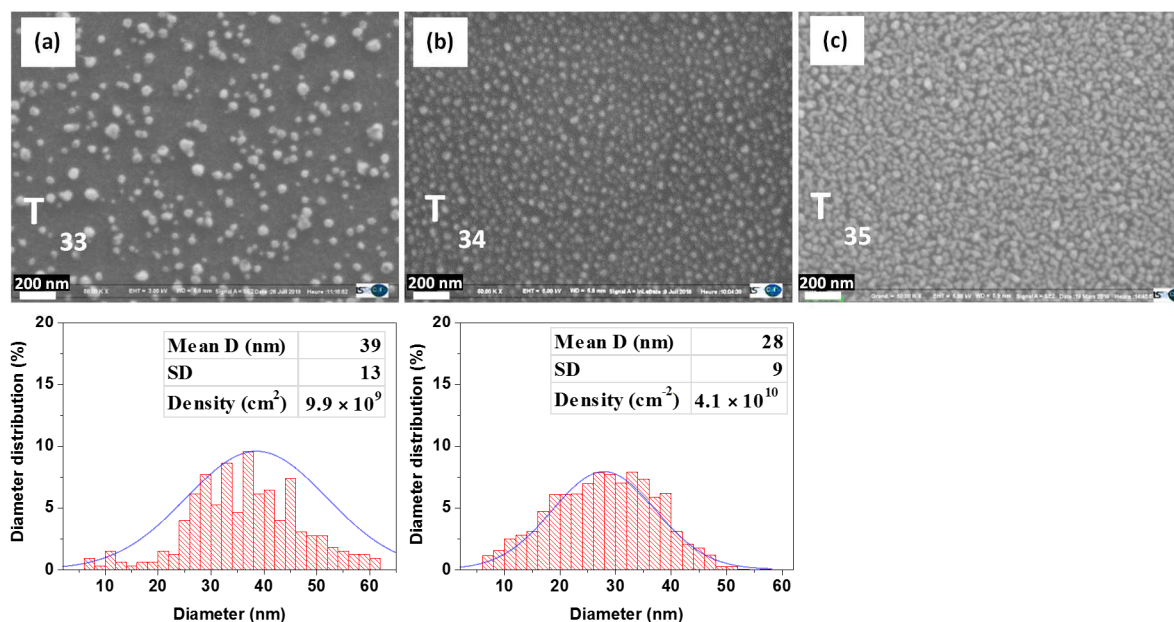


FIG. 7. SEM images and cobalt nanoparticles diameter distribution formed by dewetting on TiSiN barrier at 750°C after: (a) prolonged thermal annealing under hydrogen of 30 min (sample T₃₃) and (b) after 30 min of simultaneous thermal annealing and hydrogen plasma treatment (sample T₃₄) and (c) after 30 min of hydrogen plasma treatment only (sample T₃₅).

Nevertheless, our results demonstrate that both surface density and particle size distribution are most enhanced when protocol 2 is applied *i.e.* the plasma is applied after the formation of separate nanoparticles by thermal annealing (sample T₃₂ in Figure 6c), indeed, Bogarets *et al.* proposed recently an understanding on the effect of H radicals present in H₂ plasma on metallic nanoclusters while performing thermal annealing; these H radicals bind strongly with metallic atoms rendering them more stable. As a result, the interaction between these nanoparticles becomes very weak and they cannot coalesce [74]. Finally using only plasma treatment to dewett 3 nm cobalt films (protocol 5) has proven to be insufficient to obtain separate islands in 30 minutes (T₃₅), therefore statistical analysis was not possible, this could be explained by the weak energy furnished to the cobalt film by atomic hydrogen. Indeed, temperature monitoring on the samples surface displayed a very slow slope of rising temperature that reached 350°C at the end of the treatment.

3.3 Thickness effect

Since protocol 2 has proven the best to optimize nanoparticles size distribution, the effect of the initial film thickness on nanoparticles size distributions was investigated, we subjected 2 nm and 1 nm cobalt films deposited on TiSiN as well as SiO₂ to protocol 2. SEM images and statistical analysis of dewetted nanoparticles are shown in Figure 8. For TiSiN substrates, as represented in Figure 8.a and 8.c. Decreasing cobalt film thickness leads to an increasing in surface density, more precisely 2 nm and 1 nm thickness have improved the density by 83% and 250% respectively in comparison to 3 nm. In addition nanoparticle average size has been reduced as well to 12 nm and 8 nm for 2 nm and 1 nm initial thickness respectively, and showed more homogeneous distributions. Whereas, for SiO₂, the nanoparticle size decreasing is less obvious, as shown in Figure 8.b and 8.d. In addition, the density evolution as a function of thickness shows more or less constant values. These results are summarized in Figure 9, the model of nanoparticle size and density evolution as a function of thickness on TiSiN and SiO₂ substrates is discussed in details.

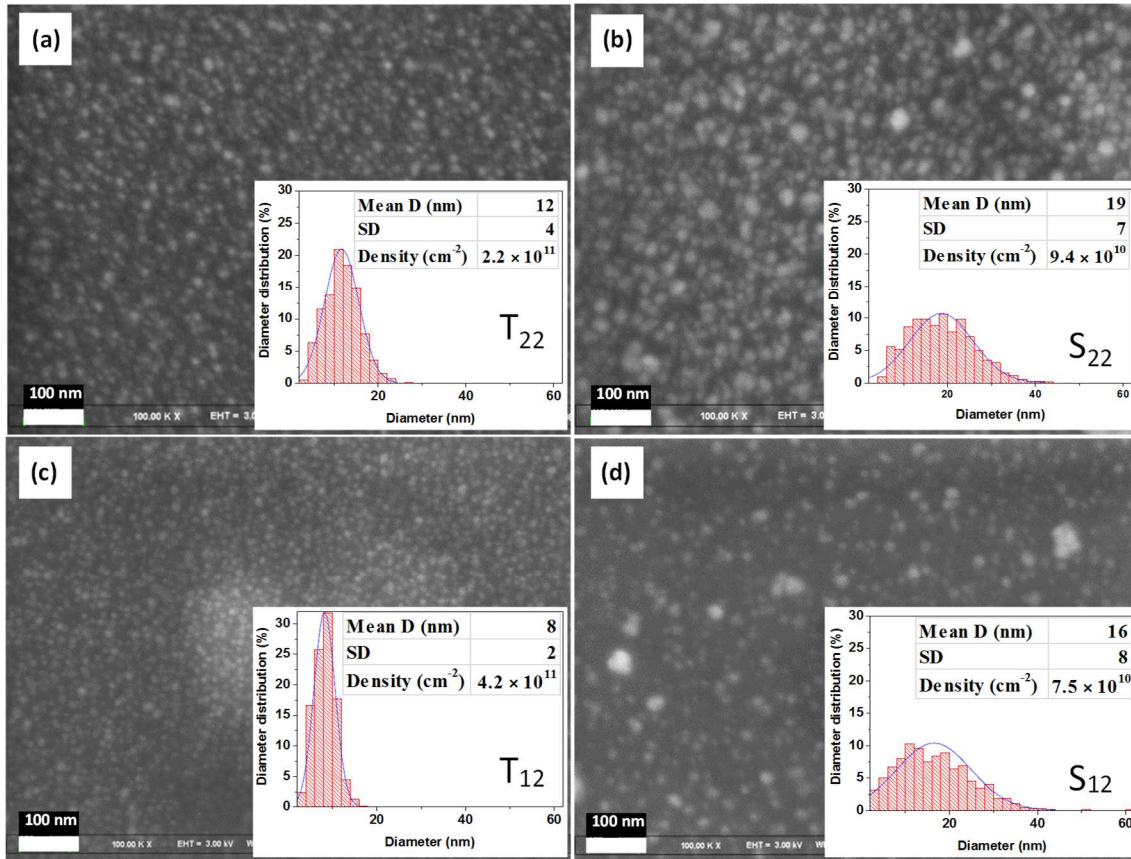


FIG. 8. SEM images and diameter distribution formed by dewetting using protocol 2 on: a) Co 2 nm on TiSiN (sample T₂₂), b) Co 2 nm on SiO₂ (sample S₂₂), c) Co 1 nm on TiSiN (sample T₁₂), d) Co 1 nm on SiO₂ (sample S₁₂).

As shown in Figure 9, TiSiN substrates display far better performances in dewetting cobalt films to form smaller, high density and homogeneous nanoparticle arrays, moreover the relationship between these three parameters are in well agreement with the model of Zhong *et al.* Although this model is limited by kinetics, the mean diameter of cobalt nanoparticles D (nm) on TiSiN shows a linear function of the initial film thickness h (nm) reaching theoretically few nanometer size nanoparticles when using sub nanometer film thickness ($D \sim 7h$), whereas cobalt nanoparticles on SiO₂ display very weak slope of a linear function with higher values that can be theoretically superior to 15 nm for sub nanometer film thickness ($D \sim 16h$). This disparity in dewetting efficiency between the two substrates is more highlighted by the surface density values. According to Zhong *et al.* model, surface density varies as function of ($N = a \cdot h^{-2}$) where a depends on the contact angle, as plotted in Figure 9.b. To describe the evolution of the model for thicknesses higher than 3 nm, larger particle size will be more likely to form by Ostwald ripening which increases with initial film thickness as clearly described by Hofman *et al.* for Co, Ni and Fe [45].

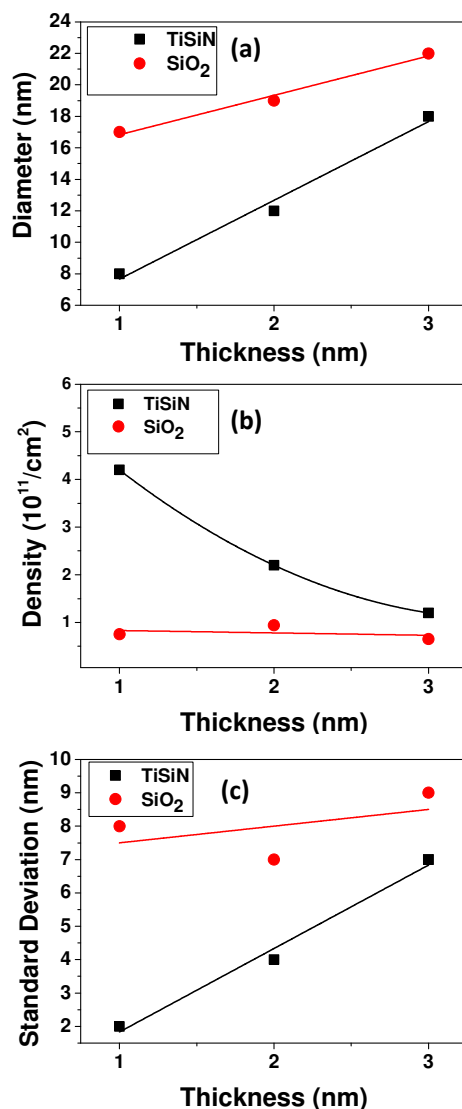


FIG. 9. Evolution of : (a) Diameter, (b) Surface density, and (c) Standard deviation of Cobalt nanoparticles as a function of initial film thickness dewetted on TiSiN and SiO₂ using Protocol 2.

The fitting curve of the density values of cobalt nanoparticles on TiSiN is in well agreement with the model. For cobalt nanoparticles dewetted on SiO₂, density values show rather fluctuating values with a maximum surface density for 2 nm, demonstrating very weak dependence between density and initial thickness. This weak dependence could be explained by the competition between two main kinetic phenomena, namely bulk diffusion and Ostwald ripening, where for thinner 1 nm film thickness bulk diffusion is most likely the dominant phenomenon resulting in smaller nanoparticles, whereas for thicker 3 nm thickness, Ostwald ripening may be the dominant phenomenon resulting in bigger nanoparticles. Though when either phenomenon is dominant, it results in low density values, the high density and low standard deviation values for 2 nm thickness could be considered as a result of the compensation between the two phenomena, *i.e.* bulk diffusion and Ostwald ripening.

3.4 Magnetic properties

We focus in this section on the static magnetic properties of the 3 nm-thick Co films on TiSiN that give a better signal-to-noise ratio than lower Co thicknesses. Figure 10 shows the normalized hysteresis curves for the as-deposited film and dewetted films, after the thermal reduction (protocol 1) and the thermal reduction associated to plasma treatment (protocol 2). They were measured in the in-plane configuration where the magnetic field is applied in the plane of the films. We focus on these two protocols, as they are representative of the effect of the thermal treatment on one side and the combination of thermal and plasma treatments on the other side. Therefore, the magnetic behavior is widely discussed based on size and shape distribution of Co nanoparticles.

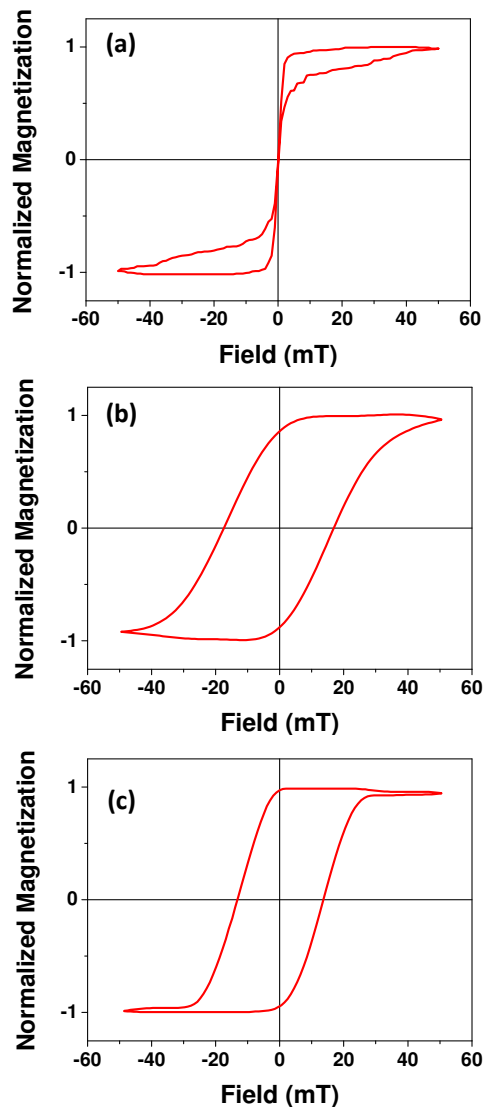


FIG. 10. Hysteresis cycles of 3 nm-thick cobalt films deposited on TiSiN: (a) as-deposited (b) after protocol 1 (heat treatment), (c) after protocol 2 (heat and plasma treatment).

The as-deposited Cobalt film presents a narrow hysteresis curve with a weak coercive field H_c about 0.6 mT. This small coercivity is probably associated with domain wall motion across grains boundaries [75]. After performing the thermal reduction (protocol 1), H_c increases to about 17 mT. As we perform the second protocol, its value decreases a little to 14 mT. The increase of the coercive field in the first protocol is due to the nanostructuring of the continuous film into nanoparticles which completely modify the magnetization reversal process. As a general trend, the coercivity is found to increase up to a maximum and then to decrease to zero with decreasing the particle size [4]. It exists a critical size, lying in the range of few tens of nanometers, which separates different magnetization behaviors. It depends on the material nature and on its micromagnetic parameters. For spherical particles, the critical diameter below which a single-domain state exists is reached when the domain-wall energy and the magnetostatic energy are equal [76]. As discussed above, introducing the plasma treatment in the second protocol produces narrow particle size distribution with higher density. This diminishes the geometrical dispersion introduced by the first protocol by exhibiting less particles side defects and more homogeneous size distribution leading to a slightly lower coercive field. The finite size effects in nanoparticles are usually illustrated through the single-domain limit and the superparamagnetic limit. In a large nanoparticle, the magnetization exhibits a multi-domains structure where uniform magnetization regions are separated by domain walls. As mentioned above, this is the results of a competition between the domain-wall energy and the magnetostatic energy. When the nanoparticle size decreases, it costs more energy to create a domain wall than to support the external magnetostatic energy. On the other hand, despite their small dimensions, nanoparticles may have a complex microstructure, as established by means of HRTEM analysis [77-79], that strongly influences the energy diagram of stationary magnetization states existing in polycrystalline nanoparticles [80]. In polycrystalline cobalt nanoparticles, in the range of diameters D between 20 and 60 nm, numerical calculations showed that above 32 nm only vortex states with low average magnetization are present, whereas below 24 nm mostly quasi-uniform states are realized in nanoparticles [80].

Considering the cobalt nanoparticles studied in this work, the size distribution provides an average size of 29 nm (with 79% of nanoparticles size above 24 nm) after performing protocol 1 and an average diameter of 18 nm (with 80% of nanoparticles size below 24 nm) after performing protocol 2, we can thus infer that these nanoparticles are mostly quasi-uniformly magnetized. The normalized remnant magnetization (M_r/M_s) exhibits values higher than 0.8. Various mechanisms can be responsible for the magnetization reversal that can correspond to coherent rotation, curling or domain wall motion. In the case of a spherical nanoparticle of diameter D , Aharoni has shown that the process of magnetization reversal by coherent rotation is ensured for up

to a diameter such that $D < D_c = 7.21 A$, A being the exchange length given by $(A/2\pi M_s^2)^{1/2}$; with A the exchange stiffness constant [81]. Namely, using the usual cobalt bulk material parameters ($A = 1.8 \times 10^{-11} \text{ J.m}^{-1}$ and $4\pi M_s = 1.76 \text{ T}$), one finds $A \approx 4 \text{ nm}$ in good agreement with literature [82]. We can conclude that the homogeneous rotation is then operative up to approximately a particle diameter of about 30 nm. The opening of the hysteresis cycles after protocol 1 and protocol 2 could be mainly attributed to a slight shift to sphericity (ellipsoidal nanoparticles). It is to mention that in the case of polycrystalline nanoparticles, an effective magnetic anisotropy can be introduced due to the fact that each nanoparticle can be represented as an assembly of monocrystalline grains of different sizes, close to the single-domain diameter, having a random distribution of their easy anisotropy [83, 84]. However, such effective anisotropy is significantly less than the anisotropy of the crystallites constituent the nanoparticle. Complex microstructure in polycrystalline nanoparticles has been presented at the origin of reduced coercive field compared with that expected from randomly oriented assembly of single-crystal nanoparticles [80]. Note also that the nanoparticles issued from protocol 1 and 2 exhibit sizes enough large to ensure that the thermal agitation does not overcome magnetic anisotropy energy; otherwise this would have led to a superparamagnetic state where the magnetization becomes unstable above the blocking temperature, leading to lack of coercivity.

4. Conclusions

Morphological and magnetic properties of dewetted Cobalt nanoparticles were investigated. The use of a TiSiN layer as an effective diffusion barrier to well control the dewetting has been proved to limit undesirable processes such as bulk diffusion and Ostwald ripening in comparison to SiO₂ surfaces. This allowed us to control the size of cobalt nanoparticles and their distribution using TiSiN combined with plasma treatment, indeed, the model of size and density evolution of cobalt nanoparticles on TiSiN as a function of initial film thickness fits perfectly with theoretical demonstrations, specific hydrogen plasma assisted dewetting protocol has been developed in order to reach optimal size and density values of 4.2×10^{11} nanoparticle per cm² with an average of 18 nm diameter. Finally, magnetic properties have been discussed within the frame of magnetic anisotropy introduced by a small deviation to sphericity of the nanoparticles. They also proved that the solid-state dewetting on TiSiN is a reliable and non-expensive approach to elaborate controlled size and distribution assembly of metal nanoparticles.

Acknowledgement

« ANR (Agence Nationale de la Recherche) and CGI (Commissariat à l'Investissement d'Avenir) are gratefully acknowledged for their financial support of this work through HEFOR and DEFISCNT projects from Labex SEAM (Science and Engineering for Advanced Materials and devices) ANR 11 LABX 086, ANR 11 IDEX 05 02 ».

References

- [1] D.L. Leslie-Pelecky, R.D. Rieke, Magnetic Properties of Nanostructured Materials, *Chemistry of Materials*, 8 (1996) 1770–1783.
- [2] R. Skomski, A. Kashyap, K.D. Sorge, D.J. Sellmyer, Multidomain and incoherent effects in magnetic nanodots, *Journal of Applied Physics*, 95 (2004) 7022-7024.
- [3] F. Fellah, S.M. Cherif, K. Bouziane, F. Schoenstein, N. Jouini, G. Dirras, Magnetic properties of ultrafine-grained cobalt samples obtained from consolidated nanopowders, *physica status solidi (a)*, 208 (2011) 1942-1949.
- [4] J.S. Lee, J. Myung Cha, H. Young Yoon, J.K. Lee, Y.K. Kim, Magnetic multi-granule nanoclusters: A model system that exhibits universal size effect of magnetic coercivity, *Scientific reports*, 5 (2015) 12135.
- [5] A.H. Lu, E.L. Salabas, F. Schuth, Magnetic nanoparticles: synthesis, protection, functionalization, and application, *Angewandte Chemie*, 46 (2007) 1222-1244.
- [6] D. Gentili, G. Foschi, F. Valle, M. Cavallini, F. Biscarini, Applications of dewetting in micro and nanotechnology, *Chemical Society reviews*, 41 (2012) 4430-4443.
- [7] M.J. Beliatis, S.J. Henley, S. Han, K. Gandhi, A.A.D.T. Adikaari, E. Stratakis, E. Kymakis, S.R.P. Silva, Organic solar cells with plasmonic layers formed by laser nanofabrication, *Physical Chemistry Chemical Physics*, 15 (2013) 8237-8244.
- [8] E.C. Dreaden, A.M. Alkilany, X. Huang, C.J. Murphy, M.A. El-Sayed, The golden age: gold nanoparticles for biomedicine, *Chemical Society reviews*, 41 (2012) 2740-2779.
- [9] M. Cavallini, F.C. Simeone, F. Borgatti, C. Albonetti, V. Morandi, C. Sangregorio, C. Innocenti, F. Pineider, E. Annese, G. Panaccione, L. Pasquali, Additive nanoscale embedding of functional nanoparticles on silicon surface, *Nanoscale*, 2 (2010) 2069-2072.
- [10] M. Gu, Q. Zhang, S. Lamon, Nanomaterials for optical data storage, *Nature Reviews Materials*, 1 (2016) 16070.
- [11] F.B. Massimiliano Cavallini, Salvador León, Francesco Zerbetto, Giovanni Bottari, David A. Leigh, Information Storage Using Supramolecular Surface Patterns, *Science*, 299 (2003) 531.
- [12] G. Chen, R.C. Davis, D.N. Futaba, S. Sakurai, K. Kobashi, M. Yumura, K. Hata, A sweet spot for highly efficient growth of vertically aligned single-walled carbon nanotube forests enabling their unique structures and properties, *Nanoscale*, 8 (2016) 162-171.
- [13] S.M. José Dintinger, Carsten Rockstuhl, and Toralf Scharf, A bottom-up approach to fabricate optical metamaterials by self-assembled metallic nanoparticles, *Optical Materials Express* 2(2012) 269-278.
- [14] C.A.R. J.Y. Cheng, E.L. Thomas, H.I. Smith, R.G.H. Lammertink, G.J. Vancso Magnetic properties of large-area particle arrays fabricated using block copolymer lithography, *IEEE Transactions on Magnetism*, 38 (2002) 2541 - 2543.
- [15] D. Gentili, F. Valle, C. Albonetti, F. Liscio, M. Cavallini, Self-organization of functional materials in confinement, *Accounts of chemical research*, 47 (2014) 2692-2699.
- [16] M. Altomare, N.T. Nguyen, P. Schmuki, Templated dewetting designing entirely self organized platforms for photocatalysis, *Chem. Sci.*, 2016, 7, , 7 (2016) 6865-6886.

- [17] R.M. Tiggelaar, R.G.P. Sanders, A.W. Groenland, J.G.E. Gardeniers, Stability of thin platinum films implemented in high-temperature microdevices, *Sensors and Actuators A: Physical*, 152 (2009) 39-47.
- [18] D. Alburquenque, V. Bracamonte, M. Del Canto, A. Pereira, J. Escrig, Dewetting of Co thin films obtained by atomic layer deposition due to the thermal reduction process, *MRS Communications*, 7 (2017) 848-853.
- [19] C.V. Thompson, Solid-State Dewetting of Thin Films, *Annual Review of Materials Research*, 42 (2012) 399-434.
- [20] J.-Y. Kwon, T.-S. Yoon, K.-B. Kim, S.-H. Min, Comparison of the agglomeration behavior of Au and Cu films sputter deposited on silicon dioxide, *Journal of Applied Physics*, 93 (2003) 3270-3278.
- [21] G. Seguíni, J.L. Curi, S. Spiga, G. Tallarida, C. Wiemer, M. Perego, Solid-state dewetting of ultrathin Au films on SiO₂ and HfO₂, *Nanotechnology*, 25 (2014) 495603.
- [22] A. Araujo, M.J. Mendes, T. Mateus, A. Vicente, D. Nunes, T. Calmeiro, E. Fortunato, H. Aguas, R. Martins, Influence of the Substrate on the Morphology of Self-Assembled Silver Nanoparticles by Rapid Thermal Annealing, *The Journal of Physical Chemistry C*, 120 (2016) 18235-18242.
- [23] S. Strobel, C. Kirkendall, J.B. Chang, K.K. Berggren, Sub-10 nm structures on silicon by thermal dewetting of platinum, *Nanotechnology*, 21 (2010) 505301.
- [24] H.J. Choe, S.H. Kwon, C. Choe, J.J. Lee, C.H. Woo, Sn microparticles made by plasma-induced dewetting, *Thin Solid Films*, 620 (2016) 165-169.
- [25] Y.J. Oh, C.A. Ross, Y.S. Jung, Y. Wang, C.V. Thompson, Cobalt nanoparticle arrays made by templated solid-state dewetting, *Small*, 5 (2009) 860-865.
- [26] A. Benkouider, A. Ronda, T. David, L. Favre, M. Abbarchi, M. Naffouti, J. Osmond, A. Delobbe, P. Sudraud, I. Berbezier, Ordered arrays of Au catalysts by FIB assisted heterogeneous dewetting, *Nanotechnology*, 26 (2015) 505602.
- [27] R. Felici, N.M. Jeutter, V. Mussi, F.B. de Mongeot, C. Boragno, U. Valbusa, A. Toma, Y.W. Zhang, C. Rau, I.K. Robinson, In situ study of the dewetting behavior of Ni-films on oxidized Si(001) by GISAXS, *Surface Science*, 601 (2007) 4526-4530.
- [28] G.G. S Hajjar, L Josien, Jean-Luc Bubendorff, D Berling, A Mehdaoui, C Pirri, T Maroutian, C Renard, D Bouchier, et al., Morphology and composition of Au catalysts on Ge(111) obtained by thermal dewetting, *Physical Review B*, 84 (2011) 125325.
- [29] C. Boragno, F. Buatier de Mongeot, R. Felici, I.K. Robinson, Critical thickness for the agglomeration of thin metal films, *Physical Review B*, 79 (2009) 155443.
- [30] A.P.W. P. R. Gadkari, R. M. Todi, R. V. Petrova, and K. R. Coffey, Comparison of the agglomeration behavior of thin metallic films on SiO₂, *Vacuum Science & Technology A*, 23 (2005) 1152-1161.
- [31] J. Cechal, J. Polcak, T. Sikola, Detachment Limited Kinetics of Gold Diffusion through Ultrathin Oxide Layers, *The Journal of Physical Chemistry C*, 118 (2014) 17549-17555.
- [32] W. Shi, J. Li, E.S. Polsen, C.R. Oliver, Y. Zhao, E.R. Meshot, M. Barclay, D.H. Fairbrother, A.J. Hart, D.L. Plata, Oxygen-promoted catalyst sintering influences number density, alignment, and wall number of vertically aligned carbon nanotubes, *Nanoscale*, 9 (2017) 5222-5233.
- [33] O. Kovalenko, E. Rabkin, Mechano-stimulated equilibration of gold nanoparticles on sapphire, *Scripta Materialia*, 107 (2015) 149-152.
- [34] H. Galinski, T. Ryll, P. Elser, J.L.M. Rupp, A. Bieberle-Hutter, L.J. Gauckler, Agglomeration of Pt thin films on dielectric substrates, *Physical Review B*, 82 (2010) 235415.
- [35] J. Ye, Fabrication of ordered arrays of micro- and nanoscale features with control over their shape and size via templated solid-state dewetting, *Scientific reports*, 5 (2015) 9823.
- [36] F. Niekiel, P. Schweizer, S.M. Kraschewski, B. Butz, E. Spiecker, The process of solid-state dewetting of Au thin films studied by in situ scanning transmission electron microscopy, *Acta Materialia*, 90 (2015) 118-132.
- [37] J. Yang, S. Esconjauregui, A.W. Robertson, Y. Guo, T. Hallam, H. Sugime, G. Zhong, G.S. Duesberg, J. Robertson, Growth of high-density carbon nanotube forests on conductive TiSiN supports, *Applied Physics Letters*, 106 (2015) 083108.

- [38] N. Na, D.Y. Kim, Y.-G. So, Y. Ikuhara, S. Noda, Simple and engineered process yielding carbon nanotube arrays with 1.2×10^{13} cm⁻² wall density on conductive underlayer at 400 °C, *Carbon*, 81 (2015) 773-781.
- [39] J. Yang, S. Esconjauregui, H. Sugime, T. Makaryan, T. Hallam, G.S. Duesberg, J. Robertson, Comparison of carbon nanotube forest growth using AlSi, TiSiN, and TiN as conductive catalyst supports, *physica status solidi (b)*, 251 (2014) 2389-2393.
- [40] C. Zhang, F. Yan, C.S. Allen, B.C. Bayer, S. Hofmann, B.J. Hickey, D. Cott, G. Zhong, J. Robertson, Growth of vertically-aligned carbon nanotube forests on conductive cobalt disilicide support, *Journal of Applied Physics*, 108 (2010) 024311.
- [41] S.J. Henley, J.D. Carey, S.R.P. Silva, Pulsed-laser-induced nanoscale island formation in thin metal-on-oxide films, *Physical Review B*, 72 (2005) 195408.
- [42] J. Bischof, D. Scherer, S. Herminghaus, P. Leiderer, Dewetting Modes of Thin Metallic Films: Nucleation of Holes and Spinodal Dewetting, *Physical review letters*, 77 (1996) 1536.
- [43] X. Hu, D.G. Cahill, R.S. Averback, Nanoscale pattern formation in Pt thin films due to ion-beam-induced dewetting, *Applied Physics Letters*, 76 (2000) 3215-3217.
- [44] T. Tanaka, J. Lee, P.R. Scheller, Interfacial Free Energy and Wettability. In : *Treatise on Process Metallurgy*, Elsevier, (2014) 61-77.
- [45] S. Hofmann, M. Cantoro, B. Kleinsorge, C. Casiraghi, A. Parvez, J. Robertson, C. Ducati, Effects of catalyst film thickness on plasma-enhanced carbon nanotube growth, *Journal of Applied Physics*, 98 (2005) 034308.
- [46] J.D. Carey, L.L. Ong, S.R.P. Silva, Formation of low-temperature self-organized nanoscale nickel metal islands, *Nanotechnology*, 14 (2003) 1223.
- [47] E. Shawat, V. Mor, L. Oakes, Y. Flegler, C.L. Pint, G.D. Nessim, What is below the support layer affects carbon nanotube growth: an iron catalyst reservoir yields taller nanotube carpets, *Nanoscale*, 6 (2014) 1545-1551.
- [48] U. Thiele, M.G. Velarde, K. Neuffer, Dewetting: film rupture by nucleation in the spinodal regime, *Physical review letters*, 87 (2001) 016104.
- [49] R. Nuryadi, Y. Ishikawa, Y. Ono, M. Tabe, Thermal agglomeration of single-crystalline Si layer on buried SiO₂ in ultrahigh vacuum, *Journal of Vacuum Science & Technology B: Microelectronics and Nanometer Structures*, 20 (2002) 167.
- [50] S.H. Kwon, D.H. Han, H.J. Choe, J.J. Lee, Synthesis of copper nanoparticles by solid-state plasma-induced dewetting, *Nanotechnology*, 22 (2011) 245608.
- [51] Y. Kojima, T. Kato, Nanoparticle formation in Au thin films by electron-beam-induced dewetting, *Nanotechnology*, 19 (2008) 255605.
- [52] G. Reiter, Dewetting of thin polymer films, *Physical review letters*, 68 (1992) 75-78.
- [53] W.W. Mullins, Theory of Thermal Grooving, *Journal of Applied Physics*, 28 (1957) 333-339.
- [54] D.J. Srolovitz, S.A. Safran, Capillary instabilities in thin films. II. Kinetics, *Journal of Applied Physics*, 60 (1986) 255-260.
- [55] G. Zhong, J.H. Warner, M. Fouquet, A.W. Robertson, B. Chen, J. Robertson, Growth of Ultrahigh Density Single-Walled Carbon Nanotube Forests by Improved Catalyst Design, *ACS nano*, 6 (2012) 2893 – 2903.
- [56] F. Maeda, H. Hibino, S. Suzuki, Y. Kobayashi, Y. Watanabe, F. Guo, Surface Reactions of Co on SiO₂ thin layer/Si substrate Studied by LEEM and PEEM, *e-Journal of Surface Science and Nanotechnology*, 4 (2006) 155-160.
- [57] L.Z. Joshua Pelleg and S. Zalkind, B. M. Ditchek, Silicide formation in the Co-Si system by rapid thermal annealing, *Thin Solid Films*, 249 (1994) 126-131.
- [58] K. Hasegawa, S. Noda, Moderating carbon supply and suppressing Ostwald ripening of catalyst particles to produce 4.5-mm-tall single-walled carbon nanotube forests, *Carbon*, 49 (2011) 4497-4504.
- [59] S.M. Kim, C.L. Pint, P.B. Amama, D.N. Zakharov, R.H. Hauge, B. Maruyama, E.A. Stach, Evolution in Catalyst Morphology Leads to Carbon Nanotube Growth Termination, *The Journal of Physical Chemistry Letters*, 1 (2009) 918-922.

- [60] X. Meng, T. Shibayama, R. Yu, S. Takayanagi, S. Watanabe, Microstructure analysis of ion beam-induced surface nanostructuring of thin Au film deposited on SiO₂ glass, *Journal of Materials Science*, 48 (2012) 920-928.
- [61] J.P. Naik, P.D. Prewett, K. Das, A.K. Raychaudhuri, Instabilities in Focused Ion Beam-patterned Au nanowires, *Microelectronic Engineering*, 88 (2011) 2840-2843.
- [62] J.D. Fowlkes, L. Kondic, J. Diez, Y. Wu, P.D. Rack, Self-assembly versus directed assembly of nanoparticles via pulsed laser induced dewetting of patterned metal films, *Nano Letters*, 11 (2011) 2478-2485.
- [63] F. Ruffino, E. Carria, S. Kimiagar, I. Crupi, F. Simone, M.G. Grimaldi, Formation and Evolution of Nanoscale Metal Structures on ITO Surface by Nanosecond Laser Irradiations of Thin Au and Ag Films, *Science of Advanced Materials*, 4 (2012) 708-718.
- [64] Sn particles produced by plasma-induced dewetting and its applications, Doctoral dissertation, (2016).
- [65] S.H. Kwon, H.J. Choe, H.C. Lee, C.W. Chung, J.J. Lee, Mechanism of Solid-State Plasma-Induced Dewetting for Formation of Copper and Gold Nanoparticles, *Journal of Nanoscience and Nanotechnology*, 13 (2013) 6109-6114.
- [66] S.-H. Kwon, H.J. Choe, H.-C. Lee, C.-W. Chung, J.-J. Lee, Control of Size Uniformity of Cu Nanoparticle Array Produced by Plasma-Induced Dewetting, *Journal of Nanoscience and Nanotechnology*, 15 (2015) 2542-2546.
- [67] J. Robertson, G. Zhong, S. Esconjauregui, C. Zhang, M. Fouquet, S. Hofmann, Chemical vapor deposition of carbon nanotube forests, *physica status solidi (b)*, 249 (2012) 2315-2322.
- [68] C.P. Lungu, I. Mustata, G. Musa, A.M. Lungu, V. Zaroschi, K. Iwasaki, R. Tanaka, Y. Matsumura, I. Iwanaga, H. Tanaka, T. Oi, K. Fujita, Formation of nanostructured Re–Cr–Ni diffusion barrier coatings on Nb superalloys by TVA method, *Surface and Coatings Technology*, 200 (2005) 399-402.
- [69] R.V. V. Ciupina, C. P. Lungu, V. Dinca, M. Contulov, A. Mandes, P. Popov, G. Prodan Investigation of the SiC thin films synthesized by Thermionic Vacuum Arc method (TVA), *The European Physical Journal D*, 66 (2012) 99.
- [70] S. Guha, A. Bandyopadhyay, S. Das, B.P. Swain, Synthesis and characterization of Titanium Silicon Nitride (TiSiN) thin film: A review, *IOP Conference Series: Materials Science and Engineering*, 377 (2018) 012181.
- [71] E. J. Lubber, B. C. Olsen, C. Ophus, D. Mitlin, Solid-state dewetting mechanisms of ultrathin Ni films revealed by combining in situ time resolved differential reflectometry monitoring and atomic force microscopy, *Physical Review B*, 82 (2010) 085407.
- [72] F. Rose, D. Pocker, Q.F. Xiao, V. Rawat, E. Brinkman, B. Marchon, Low surface energy and corrosion resistant ultrathin TiSiC disk overcoat, *Journal of Applied Physics*, 113 (2013) 213513.
- [73] F. Leroy, F. Cheynis, T. Passanante, P. Muller, Influence of facets on solid state dewetting mechanisms: Comparison between Ge and Si on SiO₂, *Physical Review B*, 88 (2013) 035306.
- [74] U. Khalilov, A. Bogaerts, S. Hussain, E. Kovacevic, P. Brault, C. Boulmer Leborgne, E.C. Neyts, Nanoscale mechanisms of CNT growth and etching in plasma environment, *Journal of Physics D: Applied Physics*, 50 (2017) 184001.
- [75] A. Kharmouche, S.M. Cherif, A. Bourzami, A. Layadi, G. Schmerber, Structural and magnetic properties of evaporated Co/Si(100) and Co/glass thin films, *Journal of Physics D: Applied Physics*, 37 (2004) 2583-2587.
- [76] X. Batlle, A.L. Labarta, Finite-size effects in fine particles: magnetic and transport properties, *Journal of Physics D: Applied Physics*, 35 (2002) R15-R42.
- [77] J. Baumgartner, A. Dey, P.H. Bomans, C. Le Coadou, P. Fratzl, N.A. Sommerdijk, D. Faivre, Nucleation and growth of magnetite from solution, *Nature Materials* 12 (2013) 310-314.
- [78] S.D. House, C.S. Bonifacio, R.V. Grieshaber, L. Li, Z. Zhang, J. Ciston, E.A. Stach, J.C. Yang, Statistical analysis of support thickness and particle size effects in HRTEM imaging of metal nanoparticles, *Ultramicroscopy*, 169 (2016) 22-29.

- [79] C. Han, D. Zhu, H. Wu, Y. Li, L. Cheng, K. Hu, TEA controllable preparation of magnetite nanoparticles (Fe_3O_4 NPs) with excellent magnetic properties, *Journal of Magnetism and Magnetic Materials*, 408 (2016) 213-216.
- [80] V.A. Bautin, A.G. Seferyan, M.S. Nesmeyanov, N.A. Usov, Magnetic properties of polycrystalline cobalt nanoparticles, *AIP Advances*, 7 (2017) 045103.
- [81] A. Aharoni, *Introduction to the Theory of Ferromagnetism*, Clarendon Press, 109 (2000).
- [82] C.D. Mee, E.D. Daniel, *Magnetic Recording*, McGraw Hill, New York, 1 (1987) 99–243.
- [83] G. Herzer, Grain structure and magnetism of nanocrystalline ferromagnets, *IEEE Transactions on Magnetics* 25 (1989) 3327-3329.
- [84] G. Herzer, Anisotropies in soft magnetic nanocrystalline alloys, *Journal of Magnetism and Magnetic Materials*, 294 (2005) 99-106.